APPLIED GEOPHYSICS, Vol.18, No.1 (March 2021), P. 117−127, 14 Figures.
DOI:10.1007/s11770-021-0881-7

Numerical modeling of anisotropy paradoxes in direct current resistivity and time-domain induced polarization methods*

Song Tao[1,2], Liu Yun♦[3], Wang Yun[2,4] and Li Bin[5]

Abstract: Based on an analytical solution for the current point source in an anisotropic half-space, we study the apparent resistivity and apparent chargeability of a transversely isotropic medium with vertical and horizontal axes symmetry, respectively. We then provide a simple derivation of the anisotropy paradoxes in direct current resistivity and time-domain induced polarization methods. Analogous to the mean resistivity, we propose a formulation for deriving the mean polarizability. We also present a three-dimensional finite element algorithm for modeling the direct current resistivity and time-domain induced polarization using an unstructured tetrahedral grid. Finally, we provide the apparent resistivity and apparent chargeability curves of a tilted, transversely isotropic medium with different angles, respectively. The subsequent results illustrate the anisotropy paradoxes of direct current resistivity and time-domain induced polarization.

Keywords: Paradox of anisotropy, direct current resistivity, time-domain induced polarization, FEM

Introduction

The direct current (DC) resistivity methods have been widely used in environmental and engineering, hydrological and mineral exploration surveys(Loke et al., 2013). Several modern DC resistivity acquiring systems can obtain time-domain induced polarization (TDIP) data and derive more useful information from underground sources (Dahlin and Loke, 2015). The modeling and inversion techniques in TDIP that are based on isotropic media are well-developed (Pelton et al., 1978; Huang et al., 2003). Anisotropy of the Earth's subsurface is universal (Linde and Pedersen, 2004); however, and existing research showed that if the electrical anisotropy of the subsurface is ignored in

Manuscript received by the editor January 21, 2019; revised manuscript received March 21, 2021.
*This research is supported by the special funding of Guiyang science and technology bureau and Guiyang University [GYU-KY-[2021]], the National Key Research and Development Program of China–Geophysical Comprehensive Exploration and Information Extraction of Deep Mineral Resources (2016YFC0600505) and the National K&D Program (2018YFC1504901, 2018YFC1504904).
1. College of Mathematics and Information Science, Guiyang University, Guiyang 550005, China.
2. State Key Laboratory of Ore Deposit Geochemistry, Institute of Geochemistry Chinese Academy of Sciences, Gui Yang 550081, China.
3. College of Earth Sciences, Yunnan University, Kunming, 650500, China.
4. School of Geophysics and Information Technology, China University of Geoscience, Beijing, 100083, China.
5. Sichuan Highway Planning, Survey, Design And Research Institute Ltd, Chengdu 610041, China.
♦Corresponding author: Liu Yun (email: yunliu@ynu.edu.cn).

the presence of inverted anisotropic data, large errors, and even false conclusions may occur (Asten, 1974; Kenkel et al., 2012). Therefore, studying the response characteristics of an anisotropic subsurface is important for understanding anisotropic media and the interpretation of anisotropic data.

Numerical simulation is the primary method used for studying the distribution law of electrical detection data and also plays an important role in understanding the physical mechanism of the method, while the forward simulation of the DC resistivity method serves as the basis of TDIP simulation. Many studies on DC resistivity anisotropic modeling have been published. One-dimensional (1D) DC resistivity layered arbitrarily anisotropic media modeling and inversion was carried out by Yin and Weidelt (1999), Yin (2000), and Yin and Maurer (2001). Additionally, three-dimensional (3D) DC resistivity modeling in anisotropic media was studied by Li and Spitzer (2005) and Zhou et al. (2009). The singularity removal technique was reviewed by Lowry et al. (1989) and Zhao and Yedlin (1996), while the mesh-generating technique was investigated by Rücker et al. (2006) and Ren and Tang (2010). Anisotropy modeling was adopted by Wang et al. (2013) to achieve a higher accuracy and modeling topography, as well as complex models.

A commonly studied and important phenomenon in the study of anisotropic media in DC resistivity modeling is known as the anisotropy paradox, a phenomenon that was verified by numerical simulations but is seldom studied in terms of its validity. Lüling (2013) provided proof of this phenomenon's existence using Coulomb's law in anisotropic media and explained this counterintuitive phenomenon using electric logging and surface surveys.

However, little research exists on anisotropic induced polarization (IP) modeling. Zhdanov (2008) introduced the generalized effective medium theory of induced polarization, which considers electromagnetic-induction and IP effects related to the relaxation of polarized charges in rock formations, and extended its use to anisotropic media (Zhdanov, 2008; Zhdanov et al., 2008). The 2D modeling technique and IP response for anisotropic complex conductivity were studied by Kenkel and Kemna (2017), Kenkel et al. (2012), and Winchen et al. (2009). These studies indicated that if anisotropic data were interpreted by isotropic inversion, a poor relationship arose with the proposed geological models, even in the presence of good data fitting. Recently, Liu et al. (2017) developed a program for modeling TDIP and FDIP responses to a 3D anisotropic medium using the finite volume method and found that the anisotropy paradox phenomenon also existed in the response of TDIP modeling.

In this paper, we provide a simple proof of the existence of the anisotropy paradoxes in direct current resistivity and TDIP and define the mean chargeability in TDIP modeling from the proof process. To verify our proof, we also developed a program for DC resistivity and TDIP modeling in 3D anisotropic medium using the finite element method with unstructured grids.

Anisotropy paradoxes in DC resistivity and TDIP methods

An analytical solution for the point source potential in an anisotropic half-space

The resistivity of an anisotropic medium can be represented by a 3 × 3 tensor, as shown in equation (1) (Yin, C., 2000; Yin, C. et al., 2018):

$$\boldsymbol{\rho_0} = \begin{pmatrix} \rho_{11} & \rho_{12} & \rho_{13} \\ \rho_{21} & \rho_{22} & \rho_{23} \\ \rho_{31} & \rho_{32} & \rho_{33} \end{pmatrix}. \tag{1}$$

The electrical potential from a current point source in an anisotropic half-space can be written as shown in equation (2) (Li and Uren., 1997a, 1997b):

$$v(r) = \frac{I_0 \left|\boldsymbol{\rho_0}\right|^{1/2}}{4\pi} \left(\frac{1}{AD_0} + \frac{1}{AD_0'} \right). \tag{2}$$

In the above equation, I_0 is the point current source $AD_0 = \sqrt{B} = \sqrt{(r-r_0)^T \cdot \boldsymbol{\rho_0} \cdot (r-r_0)}$, which can be labeled as the anisotropic distance (Lüling, 2013). This distance includes the effect of the anisotropy and is distinct from a Pythagorean distance, while AD_0' represents the anisotropic distance between the image source and the measurement point.

For the traditional DC resistivity method, the source point is located at the earth's surface; therefore, the location of the image point source is the same as for the source point, and equation (2) can be simplified into equation (3):

$$v = \frac{I_0 \left|\boldsymbol{\rho_0}\right|^{1/2}}{2\pi} \frac{1}{\sqrt{B}}. \tag{3}$$

Anisotropy paradox in DC resistivity method

By placing the current point source at $\mathbf{r_0} = (0, 0, 0)$, notation B in equation (3) can be simplified into equation (4):

$$B = \sqrt{r^T \cdot \boldsymbol{\rho}_0 \cdot r_T}. \tag{4}$$

While all three principal axes of the resistivity tensors coincided with the coordinates, the resistivity of the half-space could be expressed as $\boldsymbol{\rho}_0 = \rho_x / \rho_y / \rho_z$. Accordingly, equation (3) can be simplified into equation (5):

$$v = \frac{I_0\sqrt{\rho_x\rho_y\rho_z}}{2\pi\sqrt{\rho_x x^2 + \rho_y y^2 + \rho_z z^2}}. \tag{5}$$

For DC resistivity method, the measurement electrodes are located at the surface, and, as such, $z = 0$; then, the potential can be expressed as in equation (6):

$$v = \frac{I_0\sqrt{\rho_x\rho_y\rho_z}}{2\pi\sqrt{\rho_x x^2 + \rho_y y^2}}. \tag{6}$$

For an azimuthal anisotropy medium, when the resistivity of the x–y plane is the same, i.e., ρ_L, and the resistivity along the z-direction is ρ_T, the resistivity of the half-space can be expressed as $\boldsymbol{\rho}_0 = \rho_L / \rho_L / \rho_T$; this is also known as the vertical transverse isotropic (VTI) medium. Then equation (6) can be written as equation (7):

$$v = \frac{I_0\sqrt{\rho_L\rho_T}}{2\pi\sqrt{x^2 + y^2}}. \tag{7}$$

Equation (7) is also the analytical solution to the isotropic half-space, the resistivity of which is $\rho = \rho_m = \sqrt{\rho_L\rho_T}$. This means that, for this type of anisotropic half-space, we cannot derive any anisotropic information of the medium while the measurement electrodes are located at the surface.

For a transversely isotropic medium, while the resistivity of the x–z plane is the same, i.e., ρ_L, and the resistivity along the y-direction is ρ_T, the resistivity of the half-space can be expressed as $\boldsymbol{\rho}_0 = \rho_L / \rho_L / \rho_T$; this is also called the horizontal transverse isotropic (HTI) medium.Then equation (6) can be written as equation (8):

$$v = \frac{I_0\sqrt{\rho_L{}^2\rho_T}}{2\pi\sqrt{\rho_L x^2 + \rho_T y^2}}. \tag{8}$$

The measurement electrodes are located along the x-direction, which means the location of the measurement point is $\mathbf{r} = (x, 0, 0)$.Then equation (8) can be written as equation (9):

$$v_x = \frac{I_0\sqrt{\rho_L\rho_T}}{2\pi x}. \tag{9}$$

The above equation indicates that the measured apparent resistivity along the x-direction is $\rho = \rho_m = \sqrt{\rho_L\rho_T}$, which is the mean resistivity of the anisotropic half-space, while the true resistivity along the x-direction is ρ_L.

If the measurement electrodes are located along the y-direction, which means the location of the measurement point is $\mathbf{r} = (0, y, 0)$, equation (8) can be written as equation (10):

$$v_y = \frac{I_0\rho_L}{2\pi y}. \tag{10}$$

Equation (10) also express the potential of a half-space, while the resistivity of the half-space is ρ_L; therefore, the apparent resistivity along the y-direction is ρ_L, while the true resistivity along the y-direction is ρ_T. This is known as the paradox of anisotropy, which several scholars have verified using numerical testing (e.g., Li and Spitzer 2005; Wang. et al., 2013).

Anisotropy paradox of chargeability in TDIP method

In the finite volume algorithm for TDIP (Liu et al., 2017a, 2017b), both the resistivity and the chargeability of the medium are anisotropic and the numerical results of an HTI medium along the x- and y- are, similar to our results . That shows the anisotropic paradox of apparent resistivity. There also exists a paradox of the anisotropy-like phenomenon concerning apparent chargeability. Hereto, we provide a simple proof of the paradox of anisotropy in TDIP.

To simplify the problem, we assumed that all three principal axes of resistivity and chargeability were coincident with the coordinates. Similar to resistivity,

the chargeability tensor can be simplified as $\boldsymbol{\eta} = \eta_x / \eta_y / \eta_z$, and the apparent chargeability can be calculated by equation (11) (Oldenburg and Li, 1994):

$$\eta = \frac{v_t - v_1}{v_t}. \tag{11}$$

In the above, v_1 is the primary potential without the IP effect, and v_t is the total potential with the IP effect. For the VTI medium, where the chargeability tensor is written as $\boldsymbol{\eta} = \eta_L / \eta_L / \eta_T$, the potential without the IP effect is shown in equation (7); the potential with the IP effect is expressed as in equation (12):

$$v_t = \frac{I_0\sqrt{\rho_L'\rho_T'}}{2\pi\sqrt{x^2+y^2}}. \tag{12}$$

In equation (12), $\rho_L' = \rho_L/(1-\eta_L)$ and $\rho_T' = \rho_T/(1-\eta_T)$. If equations (7) and (12) are brought into equation (11), the following equation is derived:

$$\eta = \frac{\sqrt{\rho_L'\rho_T'} - \sqrt{\rho_L\rho_T}}{\sqrt{\rho_L'\rho_T'}}. \tag{13}$$

Equation (13) can subsequently be simplified into equation (14):

$$\eta = \eta_m = 1 - \sqrt{(1-\eta_L)(1-\eta_T)}. \tag{14}$$

The above equations indicate that the apparent chargeability is a constant. Similar to resistivity in DC resistivity method, we refer to this constant, i.e., η_m, as the mean chargeability.

For the HTI medium, where the chargeability tensor is written as $\boldsymbol{\eta} = \eta_L / \eta_T / \eta_L$, the potential without the IP effect is shown in equation (8); the potential with the IP effect is expressed as equation (15):

$$v_t = \frac{I_0\sqrt{(\rho_L')^2\rho_T'}}{2\pi\sqrt{\rho_L'x^2 + \rho_T'y^2}}. \tag{15}$$

When equations (8) and (15) are brought into equation (11), we derive the following equation:

$$\eta = 1 - \frac{\sqrt{\rho_L{}^2\rho_T(\rho_L'x^2 + \rho_T'y^2{}_L)}}{\sqrt{(\rho_L')^2\rho_T'(\rho_L x^2 + \rho_T y^2)}}. \tag{16}$$

When the measurement electrodes are located along the x-direction, the location of the measurement point is $\mathbf{r} = (x, 0, 0)$, and equation (16) can be written as equation (17):

$$\eta_x = 1 - \sqrt{\frac{\rho_L{}^2\rho_T\rho_L'}{(\rho_L')^2\rho_T'\rho_L}}. \tag{17}$$

Equations (17) can subsequently be simplified into equation (18):

$$\eta_x = \eta_m = 1 - \sqrt{(1-\eta_L)(1-\eta_T)}. \tag{18}$$

Equation (18) is the same with the mean chargeability as shown in equation (14); this phenomenon is similar to that of DC resistivity method.

Likewise, for the surveyed line along the y-direction, the apparent chargeability is shown in equation (19):

$$\eta_y = 1 - \sqrt{\frac{\rho_L{}^2\rho_T\rho_T'}{(\rho_L')^2\rho_T'\rho_T}}. \tag{19}$$

Equation (19) can subsequently be simplified into equation (20):

$$\eta_y = \eta_L. \tag{20}$$

Equation (20) implies that the measured apparent chargeability is η_L, while the true chargeability along the y-direction is η_T.

In conclusion, the above calculation tells that the measured apparent chargeability is different from the chargeability along the surveyed line in anisotropic media, this phenomenon is the paradox of anisotropy in TDIP.

The paradoxes of anisotropy in DC resistivity and TDIP are both caused by the different distribution of current density in each direction, which is also the physical basis to detect the electrical anisotropy.

Three-dimensional forward modeling of anisotropy paradoxes in DC resistivity and TDIP

The forward modeling of TDIP is based on the

simulation of DC resistivity method. The boundary value problem of the DC resistivity method with a point current source in anisotropic media is shown in equation (21) (see Wang et al., 2013; Li and Spitzer, 2005):

$$\begin{cases} \nabla\cdot(\frac{1}{\boldsymbol{\rho}}\nabla v) = -I\delta(r-r_0) & \in\Omega \\ \dfrac{\partial v}{\partial n} = 0 & \in\Gamma_s \\ \dfrac{1}{\boldsymbol{\rho}}\dfrac{\partial v}{\partial n} + qv = 0 & \in\Gamma_\infty \end{cases}. \tag{21}$$

In equation (21), $q = \dfrac{|\mathbf{r}-\mathbf{r_0}|\cos(r-r_0)\wedge n}{B}$, and $B = (\mathbf{r}-\mathbf{r}_0)^T\cdot\boldsymbol{\rho}\cdot(\mathbf{r}-\mathbf{r}_0)$.

In a study conducted by Li and Spitzer (2005), the mixed boundary condition was compared with the Dirichlet boundary condition. The mixed boundary condition is the third part shown in equation (21) define the potential on the infinite boundary Γ_∞, and Dirichlet boundary condition is generally expressed as $v = 0$ on Γ_∞ which means the potential on the infinite boundary is 0. Their result showed that the mixed boundary condition could derive better results, regardless of whether the vicinity of the source or near the boundary. Additionally, the potential using the Dirichlet boundary condition included larger errors while the measurement point is far from the source point. Accordingly, the mixed boundary condition was adopted in the simulation.

By applying equation (11), we found that dual forward modeling of the point current source was needed, once for v_1 when the resistivity was $\boldsymbol{\rho}$ and without the IP effect, and once for v_t when the resistivity was $\boldsymbol{\rho}\,[\mathbf{1}-\boldsymbol{\eta}]^{-1}$; then, the apparent chargeability could be calculated.

According to Li and Spitzer (2005), the solution for equation (21) is equivalent to minimizing the following integral:

$$\begin{cases} F(v) = \dfrac{1}{2}\displaystyle\int_\Omega\left[\nabla v\cdot(\frac{1}{\boldsymbol{\rho}}\nabla v) - 2I\delta(A)v\right]d\Omega \\ \quad + \dfrac{1}{2}\displaystyle\int_{\Gamma_\infty} qv^2 d\Gamma \\ \delta F(v) = 0 \end{cases}. \tag{22}$$

We used FEM to solve equation (22), as well as the unstructured grids created by Gmsh (v4.5.6) (Geuzaine and Remacle, 2009), which can generate high-quality tetrahedral grids and is non-commercial software. Figure 1 shows a grid generated by Gmsh; the meshes in the central area, where the electrodes are located, are refined in the image.

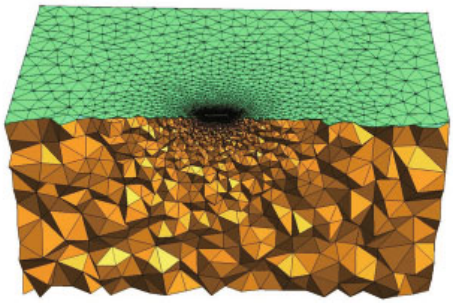

Fig. 1. Grid generated by Gmsh.

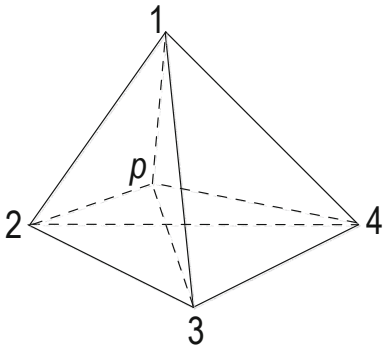

Fig. 2. Tetrahedral element.

The basic element of the grid shown in Figure 1 is tetrahedral, as shown in Figure 2.

Assuming that the electrical field at the nodes of the tetrahedral element is v_1,v_2,v_3,v_4, respectively, the potential in the tetrahedral element is linearly interpolated; then, the potential at any point in the element can be obtained by linear interpolation with the potentials of these four corner points as shown in equation (23) (Rücker et al., 2006).

$$\begin{aligned} v &= N_1v_1 + N_2v_2 + N_3v_3 + N_4v_4 \\ &= \sum_{i=1}^{4} N_iv_i = \mathbf{N^T v} = \mathbf{v^T N}. \end{aligned} \tag{23}$$

In the above equation, $\mathbf{N^T} = (N_1,N_2,N_3,N_4)$, $\mathbf{v^T} = (v_1,v_2,v_3,v_4)$ and N_i is the shape function. In the discrete element shown in Figure 1, equation (23) is placed in equation (22) to obtain the element matrix; then, the system of linear equations can be obtained by combining the element matrix shown in equation (24).

$$\mathbf{Kv} = \mathbf{P}. \tag{24}$$

After solving the linear system, the potential vector

was obtained. Based on the DC resistivity forward modeling and equation (11), we can implement the forward modeling of TDIP method by doing DC resistivity modeling twice.

Numerical tests

Verification of modeling accuracy

Figure 3 shows a two-layer model with azimuthal anisotropy, which we used to verify the correctness of our algorithm.

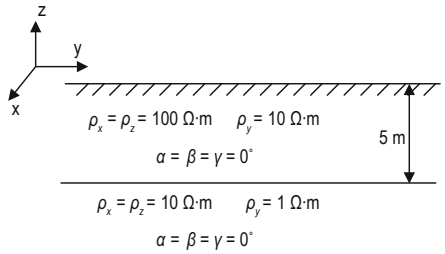

Fig. 3. A two-layered model with azimuthal anisotropy.

The principal resistivity of the first layer is $\rho_x = \rho_z = 100$ Ω·m, $\rho_y = 10$ Ω·m, and the basement half-space is $\rho_x = \rho_z = 10$ Ω·m, $\rho_y = 1$ Ω·m; for both layers, $\alpha = \beta = \gamma = 0^\circ$. The apparent resistivity of the, and the basement half-space is pole–pole array along the x-direction was calculated and compared with Li and Spitzer's (2005) solution (see Figure 4).

Our solution showed good agreement with that derived by Li and Spitzer for the entire distance of r, and the relative error was below 1%. The results showed that apparent resistivity was $\rho_a \approx 36.1$ Ω·m when the electrode spacing (r) was short, and $\rho_a \approx 36.1$ Ω·m when r was large. The apparent resistivity for short and large electrode spacing was the geometric mean of the resistivity for each layer.

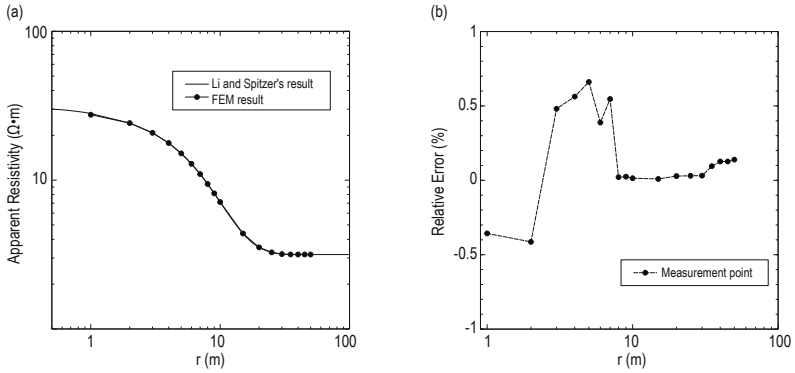

Fig. 4. Apparent resistivity and relative error of the pole–pole array along the x-direction for a two-layered model with azimuthal anisotropy, compared with Li and Spitzer's results.

Anisotropic half-space

To study the characteristics of apparent resistivity, derived from the surface resistivity survey, a half-space with azimuthal anisotropy was assumed, and the principal resistivities were $\boldsymbol{\rho_0}$ = 0.5/0.5/2.0 Ω·m, respectively. The current source and measure points are shown in Figure 5.

The Euler angles, i.e., $\beta = 0^\circ$, $\gamma = 0^\circ$ and $\alpha = 0^\circ/30^\circ/90^\circ$, respectively, were calculated separately. The measured apparent resistivity for each electrode (shown in Figure 5) of the pole–pole array is shown in Figure 6.

Where $\alpha = 0^\circ$, the apparent resistivity shown in Figure 6 presents as a circle with a radius of 1 Ω·m , equal to the mean resistivity of the anisotropic half-space; accordingly, no information about this anisotropic half-space is available. When $\alpha = 90^\circ$, the medium can be

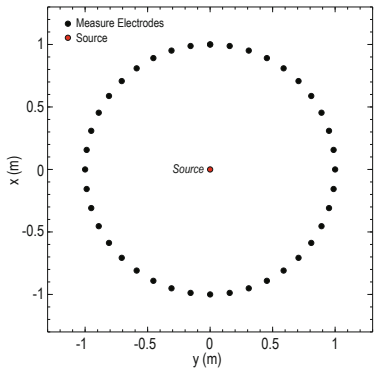

Fig. 5. Electrodes' distribution above the azimuthal anisotropy half-space. The red solid circle indicates the source electrode, which injects a current (1A) into the ground; the 41 black solid circles indicate the measurement electrodes. These measurement electrodes are distributed evenly across the circle, the center of which is the source electrode, and its radius is 1 m.

expressed as $\boldsymbol{\rho_0}$ = 0.5/2.0/0.5 Ω·m, respectively, and the apparent resistivity (Figure 6, the blue circle) presents as an ellipse with a semi-major axis equal to 1 Ω·m (x-direction), and a semi-minor axis equal to 0.5 Ω·m (y-direction); this result is consistent with the conclusion above. When α = 30°, the apparent resistivity between $\alpha = 0°$ and $\alpha = 90°$.

With the same configuration as for the homogeneous half-space, when the chargeability tensor is $\boldsymbol{\eta_0}$ = 0.1/0.1/0.6, respectively, the relevant calculated apparent chargeability is shown in Figure 7.

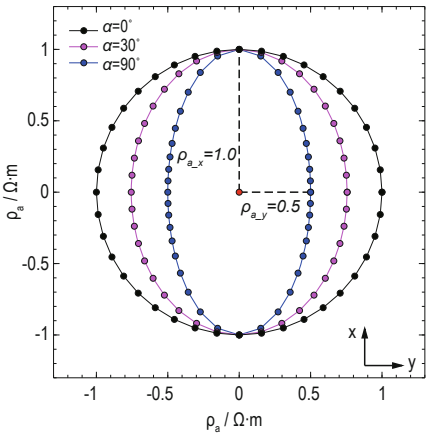

Fig. 6. Apparent resistivity of the pole–pole array for three Euler angles, i.e., α = 0°/30°/90°, respectively, while β = 0°, γ = 0°and ρ_0 = 0.5/0.5/2.0 Ω·m, respectively.The red solid circles indicate the location of the current source. The distances between the current source and other circles are the apparent resistivities, and their orientation is consistent with what is shown in Figure 5, and the same to Figure 7.

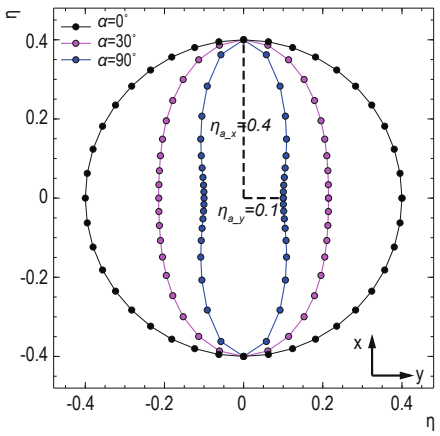

Fig. 7. Apparent chargeability of the pole–pole array for three Euler angles, i.e., α = 0°/30°/90° , respectively, while β = 0°, γ = 0°, ρ_0 = 0.5/0.5/2.0 Ω·m and η_0 = 0.1/0.1/0.6, respectively.

The curve for apparent chargeability similar to what is shown in Figure 6 and also agreed with our conclusion presented in the section discussing the paradox of anisotropy in TDIP. The calculated result represents a constant–mean chargeability of the half-space when surveying along the x-direction for three models, which in this instance is $\eta_x = 1-\sqrt{(1-0.1)\times(1-0.6)} = 0.4$. For α = 90°, the apparent chargeability is η_y = 0.1 when surveying along the y-direction.

To investigate the characteristics of mean resistivity and mean chargeability, we normalized the resistivity, i.e., ρ_L and ρ_T ranging from 0:1; then, we drew ρ_L, ρ_T and ρ_m in Figure 8.

Figure 8 shows that the mean resistivity is always close to the smaller values of ρ_L and ρ_T. The mean chargeability, i.e., η_m and η_L, is shown in Figure 9.

We found that the mean chargeability was always

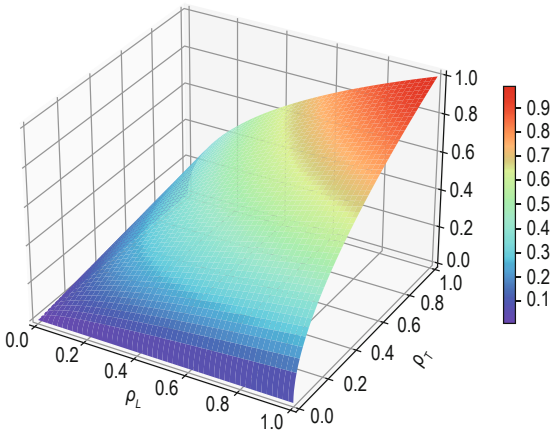

Fig. 8. Mean resistivity varies with ρ_L and ρ_T when normalizing the resistivity.

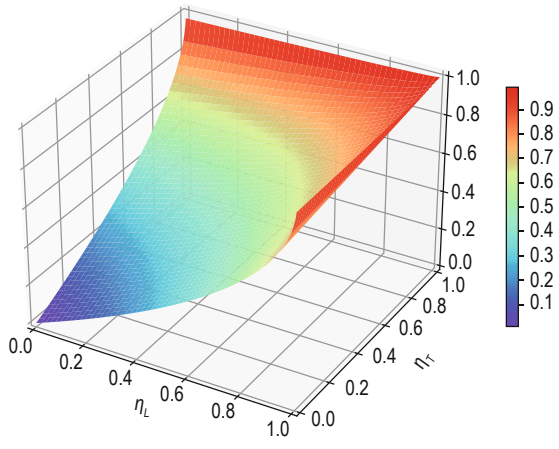

Fig. 9. Mean chargeability varies with η_L and η_T.

close to the larger values of η_L and η_T, which differed from mean resistivity.

A two-layer anisotropic model

To test our FEM code and to study the response of the layered anisotropy models, we created the model shown in Figure 10.

First, we set two Euler angles $\beta/\gamma = 0^\circ/0^\circ$; then, let α as

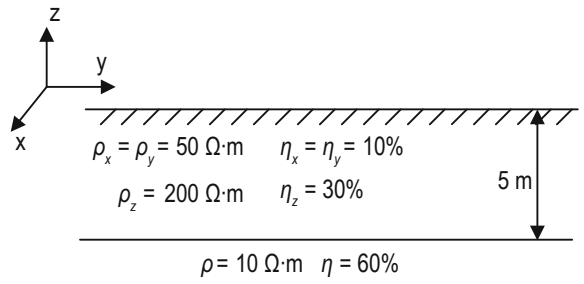

Fig. 10. A two-layer model with an anisotropic covering layer over an isotropic half-space. The three principal resistivities of the covering layer are ρ_x/ ρ_y/ ρ_z = 50/50/200 Ω·m, and the three principal chargeability values are η_x/ η_y/ η_z = 0.1/0.1/0.3. The resistivity and chargeability of the isotropic half-space are 10 Ω·m and 0.6, respectively.

0°/30°/45°/90° separately in the first layer. The apparent resistivity and chargeability of the pole–pole array along the x and y-directions are shown in Figure 11 and Figure 12, respectively.

We conclude that with large electrode spacing, all

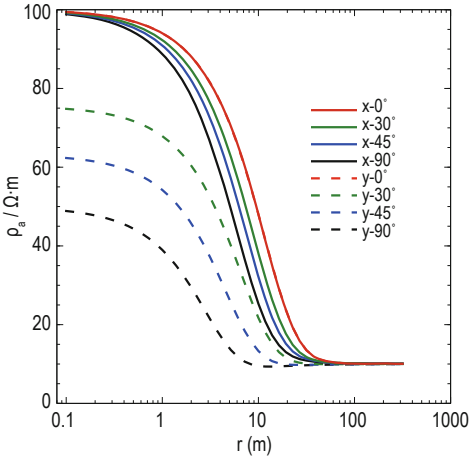

Fig. 11. Apparent resistivities along the x- and y-directions for the pole–pole array with different Euler angles.

of the measured data are close to 10 Ω·m, which is the resistivity of the isotropic half-space, and the influence of the anisotropic covering layer becomes intense when the electrode spacing is small.

When α = 0°, it is similar to the half-space model described in equation (7). With small electrode spacing, the apparent resistivity is $\rho_a \approx \sqrt{\rho_x \cdot \rho_z} = 100\Omega \cdot m$, both along the x- and y-directions, which represent the mean resistivity of the covering layer and indicates good fitting with equation (7).

When α = 90°, it is similar to the half-space model described in equation (8). With small electrode spacing, while measuring along the x-direction, the apparent resistivity is close to 100 Ω·m, which represents the mean resistivity of the covering layer and indicates good fitting with equation (9). While measuring along the y-direction, the apparent resistivity is close to 50 Ω·m, which represents the resistivity of the x-direction and is consistent with equation (10). For α = 30°/45°, the measured data are always between $\alpha = 0^\circ$ and $\alpha = 90^\circ$.

Similar to apparent resistivity, the apparent

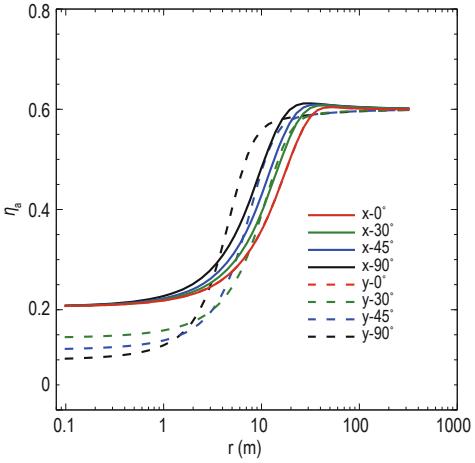

Fig. 12. Apparent chargeability along the x- and y-directions for the pole¬–pole array with different Euler angles.

chargeability (see Figure 12) shows that with large electrode spacing, all of the measured data are close to 0.6, which represents the resistivity of the isotropic half-space; the influence of the anisotropic covering layer becomes intense when the electrode spacing is small.

When α = 0°, the covering layer is the VTI. With small electrode spacing, the apparent chargeability is $\eta_a \approx 0.2$, both along the x and y-directions; this is the mean chargeability of the covering layer ($\eta_m = 1 - \sqrt{(1-0.1)\times(1-0.3)} \approx 0.2$) and indicated good fitting with equation (14).

When α = 90°, the covering layer is the HTI. With small electrode spacing, while measuring along the x-direction, the apparent chargeability is almost 0.2; this represents the mean chargeability of the covering layer and indicated good fitting with equation (18).

When measuring along the y-direction, the apparent chargeability is close to 0.1; this indicates the resistivity in the x-direction and is consistent with equation (20).

Three-dimensional anomalous target

Figure 13 shows a model of an anisotropic cube embedded in a half-space.

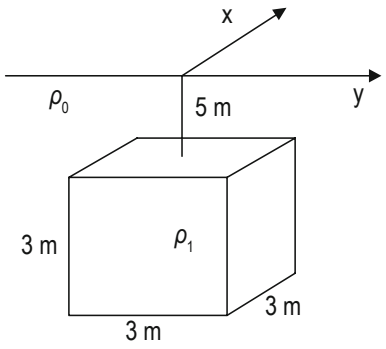

Fig. 13. A 3D anisotropic cube in a homogeneous isotropic half-space. The principal resistivity of the cube is given by ρ_{1x} / ρ_{1y} / ρ_{1z} = 100/100/500 Ω·m, and the background resistivity is ρ_0 = 10 Ω·m; the principal chargeability of the cube is given by η_{1x}/ η_{1y}/ η_{1z} = 0.6/0.6/0.3, and the background chargeability is η_0 = 0.01.

The survey line was deployed along the x-direction, and the dipole–dipole array was adopted. The Euler angles, $\alpha = \gamma = 0^\circ$, $\beta = 0^\circ/30^\circ$, and the pseudo-sections of the apparent chargeability are shown in Figure 14(a) and (b), respectively.

As shown in Figure 14, with a change in the Euler angle, the anomalous body also presents a specific angle in the apparent chargeability pseudo-section; this illustrates the influence of the anisotropic Euler angle on the observation data of the apparent chargeability. But in this model, the anisotropy paradox is not obvious.

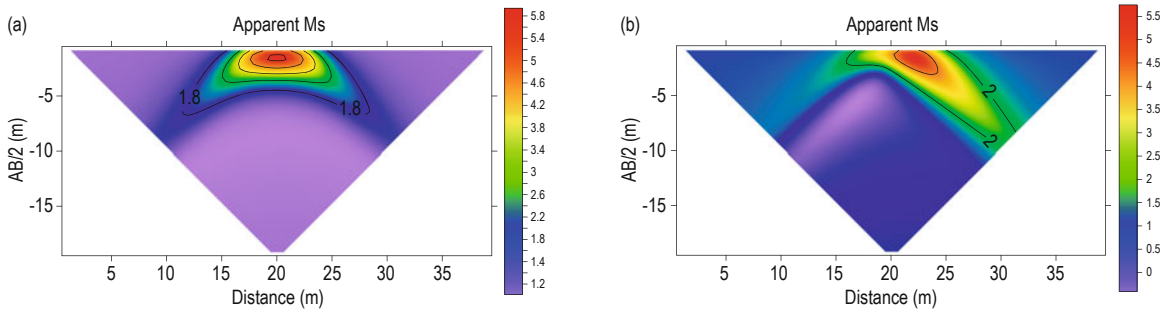

Fig. 14. Apparent chargeability pseudo-section of the model that is illustrated in Figure 13.

Conclusions

In this paper, we test and verify the anisotropy paradoxes in the DC resistivity and TDIP methods using analytical and numerical solutions. The following conclusions were drawn.

1. For the VTI medium, the apparent resistivity was consistent when measurements were made on the surface, and its value was equal to the mean resistivity of the uniform half-space; While for the HTI case, the apparent resistivity was the mean resistivity of the uniform half-space when measured along the x-direction; when measured along the y-direction, the apparent resistivity obtained was the resistivity in the x- and z-directions.

2. The definition of the mean chargeability differed from that of the mean resistivity, which is always close to the larger value of the transverse and longitudinal chargeabilities.

3. By conducting numerical simulations and analyses, the anisotropy paradoxes in resistivity and chargeability were verified, and through simulation it is found that the euler angles has a great influence on the apparent chargeabilities.

References

Asten, M. W., 1974, The influence of electrical anisotropy on Mise À La Masse surveys: Geophysical Prospecting, **22**(2), 238–245.

Dahlin, T., and Loke, M. H., 2015, Negative apparent chargeability in time-domain induced polarisation data: Journal of Applied Geophysics, **123**, 322–332.

Günther, T., Rücker, C., and Spitzer, K., 2006, Three-dimensional modelling and inversion of dc resistivity

data incorporating topography — II. Inversion: Geophysical Journal International, **166**(2), 506–517.

Geuzaine, C., and Remacle, J.-F., 2009, Gmsh: A 3-D finite element mesh generator with built-in pre- and post-processing facilities: International Journal for Numerical Methods in Engineering, **79**(11), 1309–1331

Kenkel, J., Hoerdt, A., and Kemna, A., 2012, 2D modelling of induced polarization data with anisotropic complex conductivities: Near Surface Geophysics, **10**(6), 533–544.

Kenkel, J., and Kemna, A., 2017, Sensitivity of 2-D complex resistivity measurements to subsurface anisotropy: Geophysical Journal International, **208**(2), 1043–1057

Lüling, M. G., 2013, The paradox of anisotropy in electric logging: A simple proof and extensions to other physics domains: Geophysics, **78**(1), W1–W8.

Li, P., and Uren, N. F., 1997a, Analytical solution for the point source potential in an anisotropic 3-D half-space I: Two-horizontal-layer case: Mathematical and Computer Modelling, **2**6(5), 9–27.

Li, P., and Uren, N. F., 1997b, The modelling of direct current electric potential in an arbitrarily anisotropic half-space containing a conductive 3-D body: Journal of Applied Geophysics, **38**(1), 57–76.

Li, Y., and Spitzer, K., 2005, Finite element resistivity modelling for three-dimensional structures with arbitrary anisotropy: Physics of the Earth and Planetary Interiors, **150**(1–3), 15–27.

Linde, N., and L. B. Pedersen., 2004, Evidence of electrical anisotropy in limestone formations using the RMT technique: Geophysics, **69**(4), 909–916.

Liu, W., P. Lin, Q. Lü, R. Chen, H. Cai, and J. Li., 2017, Time Domain and Frequency Domain Induced Polarization Modeling for Three-dimensional Anisotropic Medium: Journal of Environmental and Engineering Geophysics, **22**(4), 435–439.

Liu, W., P. Lin, Q. Lv, R. Chen, H. Yao, R. Shen, and H. Cai., 2017, Forward modeling of induced polarization in an anisotropic conductive subsurface: Symposium on the Application of Geophysics to Engineering and Environmental Problems 2017, 303–316.

Loke, M. H., and Barker, R. D., 1996, Rapid least-squares inversion of apparent resistivity pseudosections by a quasi-Newton method1: Geophysical Prospecting, **44**(1), 131–152.

Loke, M. H., Chambers, J. E., Rucker, D. F., Kuras, O., and Wilkinson, P. B., 2013, Recent developments in the direct-current geoelectrical imaging method: Journal of Applied Geophysics, **95**, 135–156.

Lowry, T., Allen, M. B., and Shive, P. N., 1989, Singularity removal: A refinement of resistivity modeling techniques: Geophysics, **54**(6), 766–774.

Oldenburg, D. W., and Li, Y., 1994, Inversion of induced polarization data: Geophysics, **59**(9), 1327–1341.

Qiu, C.K., Yin. C.C., Liu. Y.H., et al., 2018, 3D forward modeling of controlled-source audio-frequency magnetotellurics in arbitrarily anisotropic media: Chinese Journal of Geophysics (in Chinese), **61**(8): 3488–3498

Rücker, C., Günther, T., and Spitzer, K., 2006, Three-dimensional modelling and inversion of dc resistivity data incorporating topography — I. Modelling: Geophysical Journal International, **166**(2), 495–505.

Ren, Z., and Tang, J., 2010, 3D direct current resistivity modeling with unstructured mesh by adaptive finite-element method: Geophysics, **75**(1), H7–H17.

Sasaki, Y., 1994, 3-D resistivity inversion using the finite-element method: Geophysics, **59**(12), 1839–1848.

Wang, W., Wu, X., and Spitzer, K., 2013, Three-dimensional DC anisotropic resistivity modelling using finite elements on unstructured grids: Geophysical Journal International, **193**(2), 734–746.

Winchen, T., Kemna, A., Vereecken, H., and Huisman, J. A., 2009, Characterization of bimodal facies distributions using effective anisotropic complex resistivity: A 2D numerical study based on Cole-Cole models: Geophysics, **74**(3), A19–A22.

Yin, C., 2000, Geoelectrical inversion for a one-dimensional anisotropic model and inherent non-uniqueness: Geophysical Journal International, **140**(1), 11–23.

Yin, C., and Maurer, H. M., 2001, Electromagnetic induction in a layered earth with arbitrary anisotropy: Geophysics, **66**(5), 1405–1416.

Yin, C., and Weidelt, P., 1999, Geoelectrical fields in a layered earth with arbitrary anisotropy: Geophysics, **64**(2), 426–434.

Yin, C., Yang, Z., Liu, Y., et al., 2018, Characteristics of 3D DC Resistivity Response for Arbitrary Anisotropic Models Using Circular Scanning Measurement: Journal of Jilin University (Earth Science Edition), **48**(3):872–880.

Zhao, S., and Yedlin, M. J., 1996, Some refinements

on the finite-difference method for 3-D dc resistivity modeling: Geophysics, **61**(5), 1301–1307.

Zhdanov, M.S., 2008, Generalized effective-medium theory of induced polarization: Geophysics, **73**(5), F197–F211.

Zhdanov, M. S., Gribenko, A., Burtman, V., and Dmitriev, V. I., 2008, Anisotropy of induced polarization in the context of the generalized effective-medium theory: SEG Technical Program Expanded Abstracts 2008, 677–681.

Zhou, B., Greenhalgh, M., and Greenhalgh, S. A., 2009, 2.5-D/3-D resistivity modelling in anisotropic media using Gaussian quadrature grids: Geophysical Journal International, **176**(1), 63–80.

Song Tao, is now a lecturer at Guiyang University,

graduated from Chengdu University of Technology with a master's degree in Earth Exploration and Information Technology in 2013; graduated from Institute of Geochemistry, University of Chinese Academy of Sciences with a Ph.D. in solid geophysics in 2017. Mainly engaged in the research of geoelectric field modeling technology.

多层介质零偏VSP资料和实际零偏VSP资料，两种情况的应用进一步充分证明了LSAD_LH法的适用性和相对于LSAD法在高Q值估算的准确性，并且克服LSAD法受透射系数影响的缺点。

关键词：高低频衰减分量；品质因子；对数谱面积差

空间反射结构正则化多道反褶积//Multichannel deconvolution with spatial reflection regularization, 李皓[1,2]，李国发[1,2]，马雄[1,2]，张家良[3]，孟庆龙[3]，张祝新[3]，**APPLIED GEOPHYSICS**, 2021, **18(**1), P. 85−93. DOI:10.1007/s11770-021-0852-z

(1. 中国石油大学 (北京) CNPC物探重点实验室，北京102249；2. 中国石油大学 (北京) 油气资源与探测国家重点实验室，北京102249；3. 中国石油天然气股份有限公司大港油田分公司，天津300280)

摘要：在高分辨率地震资料处理中通常采用稀疏脉冲反褶积方法来展宽地震数据的有效频带，增强地震数据刻画薄层结构的能力。但是，现有的稀疏脉冲反褶积方法采用逐道运行模式，未考虑地震信号在相邻道之间的空间约束关系。受高频噪声的影响，反褶积结果不仅具有较强的多解性，且降低了地震信号的空间连续性。为此，本文提出了一种空间反射结构正则化多道稀疏脉冲反褶积方法。该方法从地震数据本身提取空间反射结构表征算子，将表征算子引入到多道稀疏脉冲反演的正则化条件，增强了稀疏脉冲反褶积方法的抗噪性和稳定性。理论模型实验和实际资料处理证实了该方法的正确性和可行性。

关键词：反褶积，空间结构约束，分辨率，稀疏脉冲

基于海森矩阵因数分解的最小二乘逆时偏移方法研究//Least-squares reverse time migration method using the factorization of the Hessian matrix, 孙小东[1,2], 腾厚华[3]，任丽娟[4]，王伟奇[1]，李振春[1]，**APPLIED GEOPHYSICS**, 2021, **18(**1), P. 94−100. DOI:10.1007/s11770-021-0853-y

(1. 深层油气重点实验室，中国石油大学 (华东)，青岛 266580；2. 山东省油藏地质重点实验室，中国石油大学 (华东)，青岛 266580；3. 中国石化胜利油田有限公司物探研究院，东营 257022；4. 中海石油 (中国) 有限公司湛江分公司, 湛江 524000)

摘要：最小二乘偏移基于反演的思想，通过迭代的方式逐步消除成像假象，恢复成像振幅，最终提供高分辨率的成像剖面，而且能够处理不完备、低品质的地震数据。基于双程波波动方程进行波场外推可以实现高陡构造及逆掩断层的成像，但是庞大的计算量限制了最小二乘逆时偏移的应用。为了解决计算量的问题，本文提出一种成像域的快速算法，以提高最小二乘逆时偏移的计算效率。该方法借助于克罗内克积叠加的因数分解算法来估算海森矩阵,实现了海森矩阵的低秩分解。克罗内克因子的求取只涉及到计算炮点和检波点处的格林函数，从而避免了直接构建整个海森矩阵。因此，基于因数分解的最小二乘逆时偏移采用低秩矩阵的乘法， 避免了耗时的偏移和反偏移过程。模型和实际资料的处理验证了该方法在计算效率方面的优势。在取得相同效果的基础上，基于因数分解的最新二乘逆时偏移耗时约为常规最小二乘逆时偏移的一半，这在工业界应用时可以显著降低计算成本。因数分解方法引起的噪音可以通过常规滤波手段去除，不会降低成像质量。

关键词：最小二乘，逆时偏移，因数分解，Hessian矩阵

地—井瞬变电磁三维非结构有限元正演模拟研究//Three-dimensional forward modeling for the SBTEM method using an unstructured finiteelement method, 王路远[1]，殷长春[1]，刘云鹤[1]，苏扬[1]，任秀艳[1]，惠哲剑[1]，张博[1]，熊彬[2]，**APPLIED GEOPHYSICS**, 2021, **18(**1), P. 101−116. DOI:10.1007/s11770-021-0863-9

(1. 吉林大学地球探测科学与技术学院，长春 130026；2. 桂林理工大学地球科学学院，桂林 541004)

摘要：为分析复杂地电模型条件下地—井瞬变电磁响应特征，本文基于非结构网格矢量有限元法实现了时间域地—井瞬变电磁三维正演模拟。为求解双旋度电场扩散方程，我们使用非结构四面体网格对计算空间进行离散，同时选择无条件稳定的后退欧拉方法进行时间离散。数值实验中我们首先以长导线源为例分析电性源电磁场分量的扩散特征和探测能力；然后重点研究Ex、dBy/dt零值带的产生机理及分布规律。目标在于指导实际地—井电磁探测中选择合理的测量区域。最后，我们通过模拟复杂模型的异常特征，分析地—井瞬变电磁法探测典型脉状矿体的可行性，为深部矿产资源探测提供参考。

关键词：地—井瞬变电磁，正演模拟，矢量有限元，非结构网格，零值带

直流电阻率法和时间域激发极化法各向异性反常现象数值模拟//Numerical modeling of anisotropy paradox in direct current resistivity and time-domain induced polarization methods，宋滔[1,2]，刘云[3]，王赟[2,4]，李斌[5]，**APPLIED GEOPHYSICS**, 2021, **18(**1), P. 117−127. DOI:10.1007/s11770-021-0881-7

(1. 贵阳学院数学与信息科学学院，贵阳 550002；2. 中国科学院地球化学研究所，矿床地球化学国家重点实验室；3. 地球科学学院，云南大学，昆明 650091；4. 地球物理与信息技术学院，中国地质大学 (北京)，北京 100083；5. 四川省公路规划勘察设计研究院有限公司，成都 610041)

摘要：本文基于点源场均匀半空间各向异性介质的解析解，研究了横向同性介质中电性对称轴分别为垂直和水平时地表测量的视电阻率和视极化率特点，证明了关于电阻率和极化率各向异性反常现象，并类比于平均电阻率提出了一种横向同性介质中平均极化率的计算方式。本文进一步基于有限单元法实现对时间域激发极化法三维正演计算，其中使用非结构四面体单元剖分灵活地实现了对任意极距的模拟。通过模拟对称轴倾角不同的横向同性介质，验证了本文关于各向异性反常现象的讨论。

关键词：各向异性反常, 直流电阻率法, 时间域激发极化法, 有限单元法